

A Metallurgical Investigation of the Direct Energy Deposition Surface Repair of Ferrous Alloys

Manuel Marya, Virendra Singh, Jean-Yves Hascoet, and Surendar Marya

(Submitted June 26, 2017; in revised form December 13, 2017; published online January 5, 2018)

Among additive manufacturing (AM) processes, the direct energy deposition (DED) by laser is explored to establish its applicability for the repair of ferrous alloys such as UNS G41400 low-alloy steel, UNS S41000 martensitic stainless steel, UNS S17400 precipitation-strengthened martensitic stainless steel, and UNS S32750 super-duplex stainless steel. Unlike plating, thermal spray, and conventional cladding weld, DED laser powder deposition offers potential advantages, e.g., thin deposits, limited dilutions, narrow heat-affected zones (HAZ), potentially improved surface properties. In this investigation, all AM deposits were completed with an IREPA CLAD™ system using a powder feed of UNS N06625, an alloy largely selected for its outstanding corrosion resistance. This investigation first addresses topological aspects of AM deposits (including visual imperfections) before focusing on changes in microstructure, microhardness, chemical composition across AM deposits and base materials. It has been established that dense, uniform, hard (~ 300 HVN), crack-free UNS N06625-compliant AM deposits of fine dendritic microstructures are reliably produced. However, except for the UNS S32750 steel, a significant martensitic hardening was observed in the HAZs of UNS G41400 (~ 650 HVN), UNS S41000 (~ 500 HVN), and UNS S17400 (~ 370 HVN). In summary, this investigation demonstrates that the DED laser repair of ferrous parts with UNS N06625 may restore damaged surfaces, but it also calls for cautions and complementary investigations for alloys experiencing a high HAZ hardening, for which industry standard recommendations are exceeded and lead to an increased risk of delayed cracking in corrosive environments.

Keywords additive manufacturing, dilution, hardness, heat-affected zone, microstructures, UNS G41400, UNS S41000, UNS S17400, UNS S32750, UNS N06625

1. Introduction

Additive manufacturing (AM) has been transforming industries where small volumes of intricate parts, as well as short lead time, are important to end-users (Ref 1-6). In contrast to machining, AM produces parts by successive layering of one or several materials utilizing a growing number of innovative technologies (Ref 4). For metallic parts, Binder Jet, directed energy deposition (DED) and powder bed fusion have slowly claimed their own share of the AM market (Ref 4). The DED process normally utilizes metals (alloys) that are powder-fed and melted by an energy source, commonly a laser beam (Ref 4, 5, 7). Compared to alternate AM processes, the DED process is better aligned with the manufacturing and size constraints of large and heavy oil field mechanical parts. For repairing such parts, DED enables precise powder feed delivery at low-energy density, therefore promoting controlled base material dilutions, small heat-affected-zones (HAZ), and minimal part distortions and cracking (Ref 8). Recently, the repair of mechanical parts by AM has received interests from the oil and gas industry due

to rapid customization needs, longer-than-desirable lead times, and specialized labor shortages nearby rig locations (Ref 8). The DED family of processes, especially utilizing lasers, is complementary to today's processes for repairing parts, particularly for those in need of thin deposits otherwise achieved by plating or thermal spray. Unlike the latter processes, AM deposits are advantageously fused to the base materials, therefore far less susceptible to spalling (flaking). In comparison with conventional welding, smaller HAZs and limited dilutions are additional potential benefits that are also imperative to establish in this investigation.

In this paper, the DED laser powder deposition is applied on several typical ferrous alloys found in today's exploration and production equipment. Low-alloy steels such as UNS G41400 (4140) and equivalent grades listed by the American Petroleum Institute (API) are industry workhorses at yield strengths between 550 MPa (80 ksi) and 860 MPa (125 ksi). Being a low-alloy chromium-molybdenum steel, UNS G41400 is inherently prone to various forms of corrosion at surface as well as downhole environments. These mainly include uniform corrosion, pitting corrosion, and crevice corrosion. Higher-strength grades may be subject to elevated tensile stresses, the latter developing into cracking in sour fluids and completion brines. In typical exploration and production equipment, UNS G41400 is quenched and tempered to develop a microstructure with balanced strength, toughness, and corrosion resistance. Differently, stainless steels such as UNS S41000 (410, 13Cr), UNS S17400 (17-4PH, Alloy 630), UNS S32750 (25Cr), and nickel-base alloy UNS N06625 (625) are often referred as to corrosion resistant alloys (CRA). UNS S41000 is a quenched and tempered martensitic stainless steel with 11.5-13.5 wt.% chromium that combines minimal corrosion resistance and minimal strength for pressure vessel applications (i.e.,

Manuel Marya and Virendra Singh, Schlumberger Technology Corporation, 14910 Airline Road, Rosharon, TX 77583; and Jean-Yves Hascoet and Surendar Marya, Ecole Centrale Nantes, 1 Rue de la Noë, 440872 Nantes Cédex, France. Contact e-mails: mmarya@slb.com and VSingh10@slb.com.

550 MPa, 80 ksi). UNS S41000 is known to be susceptible to both pitting (PREN ~ 12) and cracking in sour and chloride environments, including completion brines (Ref 9, 10). UNS S17400, commonly refers as 17-4PH, is a martensitic precipitation-hardening (PH) stainless steel with PREN > 16, 15.0-17.5 wt.% chromium, 3.0-4.5 wt.% of both nickel and copper, 0.15-0.45 wt.% niobium, and is generally used where a higher strength is desirable. Depending upon precipitation aging treatment, UNS S17400 is encountered between 720 MPa (105 ksi in the HH1150 condition) and 1100 MPa (160 ksi in the H900/H925 conditions) and characteristically suffers from poor cracking resistance in oil field environments. For temporary service where risk of cracking is negligible, UNS S17400 is substituted or restricted by operational stresses and/or alloy strength, as per the HH1150 heat treat condition. Unlike previous stainless steels aforementioned, UNS S32750 is a heat-treated alloy with approximately 24.0-28.0 wt.% chromium, 6.0-8.0 wt.% nickel, 3.0-5.0 wt.% molybdenum, and 0.24-0.32 wt.% nitrogen that stabilizes a dual austenite-ferrite microstructure with excellent corrosion resistance. Among commercial CRAs, the super-duplex stainless steels have the highest pitting resistance equivalent numbers (PREN > 40) and therefore are also best suited to chloride environments. However, their cracking resistance in sour environments remains greatly limited, as is their corrosion resistance in mineral acids. In this investigation, all oil field alloys were selected to meet the metallurgical requirements of NACE MR0175/ISO15156, particularly the maximum hardness criteria (Ref 9). The potential consequences of having any major base material hardening under AM deposits exacerbated by undesirable chemical interactions between AM material and base materials weighed heavily on this investigation, particularly for the steels with martensitic transformations.

The alloy, referred to as UNS N06625 (Alloy 625, Inconel 625™), is a low-carbon austenitic Ni-Cr-Mo-Nb alloy and as such outperforms the previously mentioned alloys in corrosive environments. UNS N06625 is a non-magnetic Ni-Cr-Mo nickel-based superalloys strengthened mainly by solid-solution and, to a minor extent, the precipitation of Ni₃Nb. The PREN of UNS N06625 is in excess to that of super-duplex stainless steels, a distinctive characteristic that has widespread the use of UNS N06625 in the oil and gas industry. In contrast to stainless steels, UNS N06625 is practically immune to all oil field environments despite standard restrictions for permanent sour service (Ref 9). Historically, UNS N06625 has been a well-established alloy for weld overlays and thermal sprays to supplement or repair mechanical parts. When applied as an AM powder in rapid solidification conditions, UNS N06625 is anticipated to enhance surface characteristics of both low-alloy steels and stainless steels and as such extend the lives of worn-out oil field assets that would be otherwise scrapped. In many cases, the outstanding corrosion resistance of UNS N06625 is likely to make repaired parts more robust to a multitude of environments. Through the metallurgical investigation of AM deposition onto various oil field alloys, the technical potential of AM for repair is being evaluated.

1.1 Experimental Procedure

The DED laser deposition repair of UNS G41400, UNS S41000, UNS S17400, and UNS S32750 by UNS N06625 was investigated utilizing rectangular test samples (80 mm × 20 mm × 7.5 mm). Samples were procured from Metal Samples

(<http://www.alspi.com>) in required heat treat condition. Criteria for a successful AM deposit were established as (1) a base material matching hardness for comparable abrasive wear properties and (2) an improved corrosion resistance for durable oil field services (as measured by PREN). Since among all three base materials, UNS S32750 (PREN ~ 42.4) is best suited for chloride environments, it was established that proper AM deposits should consistently match a minimum PREN value of 40, therefore having a chemical composition similar to UNS N06625 (i.e., insignificant dilution). Table 1 shows the manufacturer-certified powder chemical composition and its derived PREN, as calculated by the NACE MR0175/ISO15156 PREN formula (Ref 9). Compared to standard UNS N06625 wrought products, the UNS N06625 powder is oxygen-enriched, as intrinsically expected from powders (high surface-to-volume ratio), yet its PREN value is 53, well exceeding the minimum established requirement in this investigation. Also, note that carbon is absent to avert undesirable carbides, which can cause sensitization in any diluted zone. For superior flow and packing properties, the selected powder was inert gas atomized. As indicated in Fig. 1(a), this powder is spherical and characterized by a narrow particle size range between 45 and 70 μm to help establish a stable deposition stream.

The DED laser powder deposition was accomplished using a customized 3D-printer, referred as CLAD™, and depicted in Fig. 1(b). The CLAD AM printer is a modified IREPA fiber laser system (France) of 4 kW with a highly tunable output power for thin deposits (Ref 11). In the IREPA CLAD system, the powders are fed coaxially into the optical lens focal point at a controlled rate to promote a stable powder stream, as illustrated in Fig. 1(c) and (d). Optical images such as in Fig. 1(d) are intermittently captured as a mean of monitoring powder feed, which when compromised indicates an unsteady powder deposition.

Figure 1(e) shows top views of AM test samples having parallel lines of fused UNS N06625 powder. As standard test procedure, the AM deposits were first examined using a Keyence VHX100 microscope with 3D topographic capabilities, then quantitatively analyzed. A total of 8 test samples (2 per alloy) were examined. The samples were then cross-sectioned, mounted, polished, and etched to reveal their microstructures, particularly across AM deposit and base material interface (fusion line). Etching was accomplished using reagents tailored to the base materials, (i.e., for UNS G41400 the reagent was Nital 2% nitric acid in ethanol), while for both UNS S41000 and UNS S17400 it was Vilella's reagent (e.g., 100 cc hydrochloric acid, 100 cc ethanol, 2 g picric acid). For UNS S32750, the high PREN required an electrolytic etching in a solution consisting of 40 g sodium hydroxide in 100 ml of distilled water. Following etching, the AM test samples were examined by optical microscopy, scanning-electron microscopy (SEM), and electron-dispersive spectroscopy (EDS). Vickers microhardness (HV) profiles under 100 g loads were measured from AM deposit top surfaces down to base materials. The 100-g indentation load was selected to reveal sufficient changes in hardness and microstructures across AM deposits and base materials. Complementarily, notched-test samples were prepared for 90° bend testing to assess relative cracking resistance, in particular toward interfacial cracking. The bend test samples were prepared by sectioning AM test samples such as in Fig. 1(e) and then fine cutting by a diamond blade a notch of 880-μm-radius and 1600-μm-wide on the base materials, implicitly

Table 1 Nominal chemical composition of the UNS N06625 powder (in wt.%)

Ni(a)	Cr	Fe	Nb	Mo	Mn	Si	Ti	N	O	PREN(b)
Bal	21.40	6.50	3.33	9.10	0.41	0.43	0.09	0.11	0.05	53.2

(a) Per UNS N06625 composition, minimum nickel is 58 wt.%. (b) PREN = 1% Cr + 3.3 (%Mo + 0.5% W) + 16% N (Ref 9)

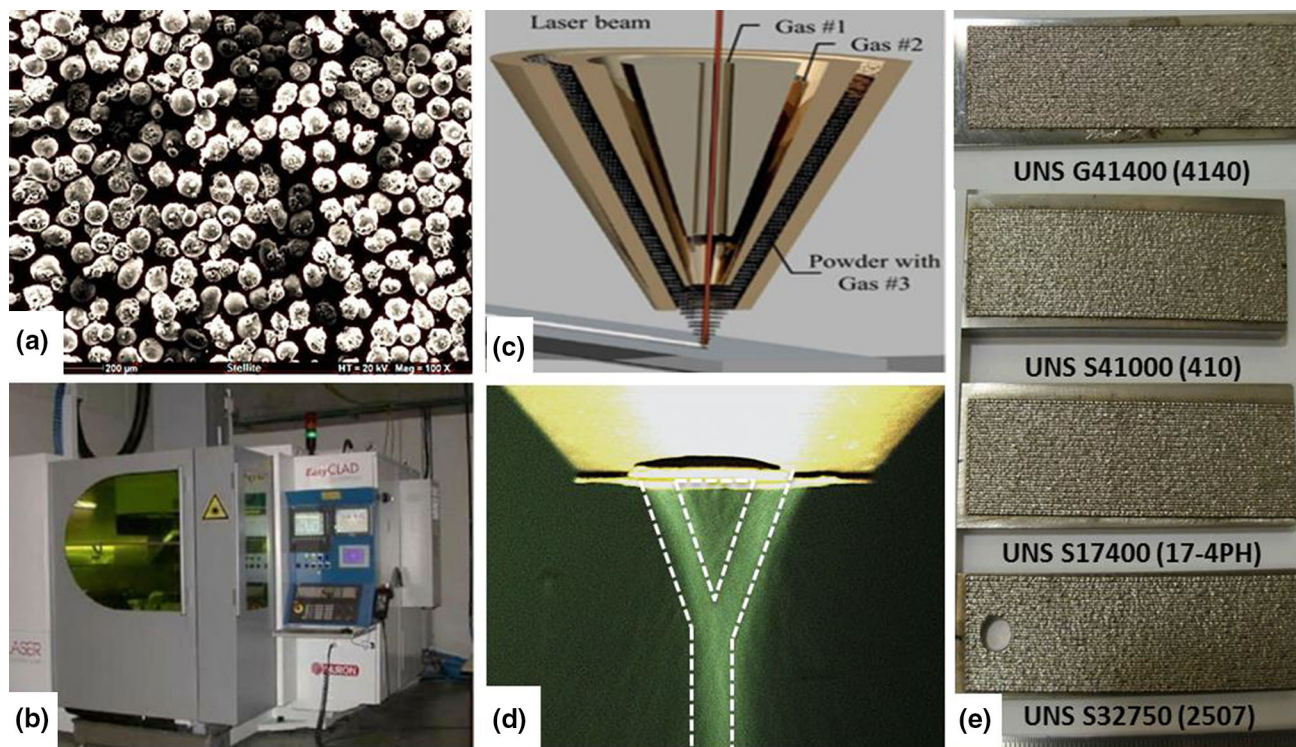


Fig. 1 (a) SEM image of the used UNS N06625 powder, (b) photograph of the CLAD AM system (ECN, France), (c) schematic illustration of the powder feed nozzle, (d) photograph of a powder cone reaching minimum diameter by the optical lens focal point, and (e) examples of rectangular test samples

leaving the AM deposits under a dominant compressive state of stress. This bend test is based on ASTM B571 (Ref 12) for evaluating plating adhesion, but with the introduction of a notch and the AM deposit in compression, the intent of this modified test was to promote tensile stresses at or nearby the HAZ, where cracking had a greater probability of occurring. Properly positioning the notch was challenging, resulting in sample-to-sample variability. The notches were set to penetrate 6.5 mm into the test samples so that they would be within 1 mm from the AM deposits with estimated variations of 250 μ m. This bend testing was only for screening and comparison purposes.

In the CLAD system, laser beam head height, powder delivery rate, and turntable position are adjusted real-time to enable complex scan paths. In this investigation, all test samples had two layers applied in a crosshatched pattern, as depicted in Fig. 2. To demarcate each consecutive layer, contouring passes were superimposed, resulting in thicker deposits along the sides. To minimize gaps between paralleled line scans (Ref 8, 11, 13, 14), all line scans were 0.5 mm apart. Correspondingly, the second layer was made with the powder feed moved upward by only 0.2 mm relying on past successful

AM deposition (Ref 11, 13, 14). Table 2 summarizes the AM process parameters of this investigation. Two scan speeds were utilized to address the concern for potential. Much of the results in this paper remain associated with the 800 mm/min scan speed. In Table 2, the deposition rate is calculated as opposed to directly measured.

2. Results and Discussion

In this section, the following are discussed: (1) visual appearance of the AM deposits, (2) cross section microstructures, particularly across AM deposit-base material interfaces, (3) microhardness across various metallurgical zones to address concerns over brittle and cracking-susceptible microstructures, (4) compositional analyses to evaluate the dilution (mixing) between powder feed and base materials, therefore determining potential changes in corrosion resistance over that of UNS N06625, and (5) simple bend tests to further address the brittleness concerns, especially for the alloys with martensitic transformations.

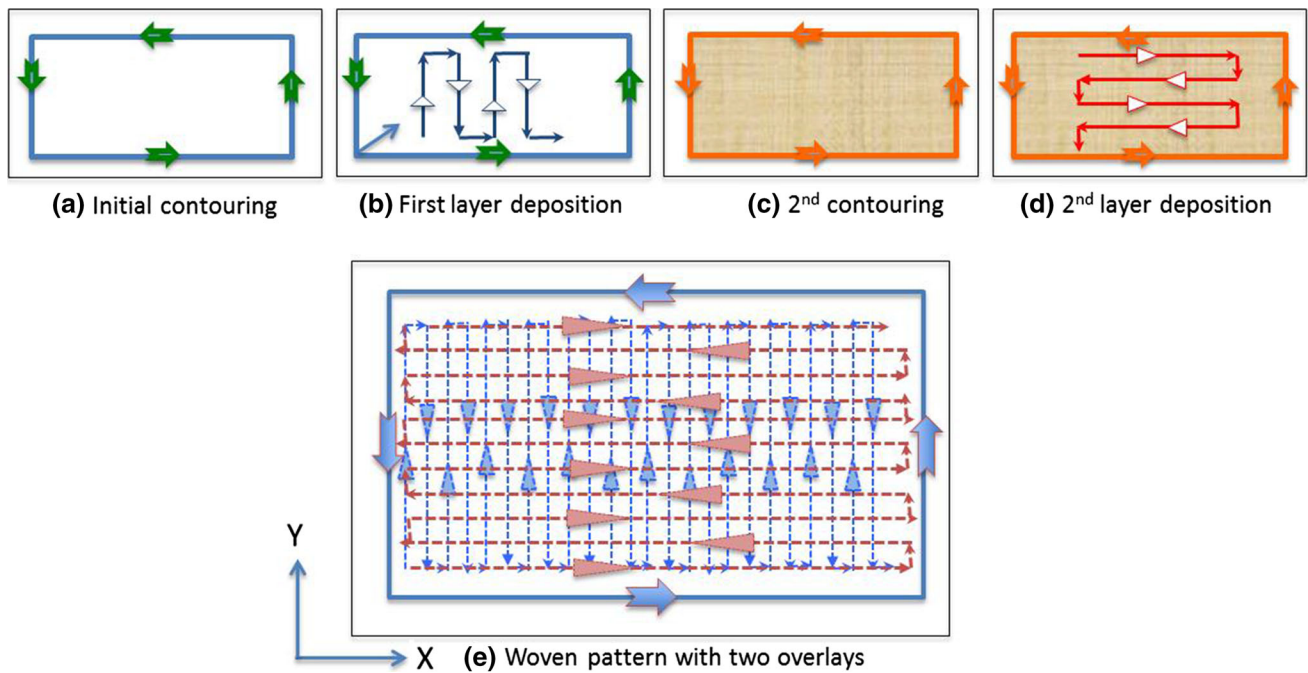


Fig. 2 Schematic representation of the AM deposition pattern: (a) and (b) for the first layer; (c) and (d) for the second and last layer; (e) composite pattern superimposing the complex scan path from beginning to end and aimed at providing full area coverage

Table 2 Summary of AM process parameters

Beam power, W	Scan speed, mm/min	Focal diameter, mm	Gas #1 and #2 flow rates, L/min	Gas #3, L/min	Number of layers	Deposition rate, g/min
180	600 and 800	0.56	2.9 and 1.5	3.5	2	0.75-0.80

2.1 Visual Appearance

Figure 3 shows a set of 3D topological images for several AM deposits in all four base materials, starting with the low-alloy steel (Fig. 3a) and ending with the super-duplex stainless steel (Fig. 3d). At first glance, all four views appear identical, each displaying five parallel fused lines with slight differences, e.g., variations in line widths indicative of an unsteady AM deposition. The AM fused lines in Fig. 3(a), (b), (c), and (d) are irregular and show slightly different heights with peaks and valleys, but for the most part, are seemingly protective of the base materials with no gaps between fused lines. Over all surfaces of the AM deposits, residual powders associated with a partial powder feed melting are seen. Digital image analyses revealed 80 ± 4 powder particles per image, therefore indicating an invariant statistical population. Despite processing setup precautions regarding powder and process variable selection (reused from past successful work) (Ref 11, 14), the powder stream (Fig. 1d) is still subject to variations, resulting in AM deposit profile differences and potentially internal defects. Slight variations in powder chemistry and beam-metal absorption are known to influence melt composition, flow dynamics, and interfacial phenomena, including solid-liquid wetting contact angles. Published literature on the role of surface tension on melt morphology, as related to chemistry variations and related Marangoni-induced flow (e.g., ppm of sulfur, oxygen), is quite extensive (Ref 13, 15, 16). Lower surface tension along with negative temperature gradient tends to

promote outward fluid flow, which may be associated with flatter fused lines supporting greater line overlaps. Since the AM fused lines of Fig. 3 are convex compared to past work (Ref 8, 11, 13, 14), laser beam and powder feed did unlikely maximize AM deposit area coverage. By reducing scan rate and/or increasing beam power, essentially raising the heat input and melt temperature, the AM fused lines could have been flattened further and exhibit less residual powders. As a downside, increasing heat input would have augmented dilution (mixing) of the first AM layer with the base materials, therefore introducing further metallurgical changes. With residual powders over the fused lines, as shown in Fig. 3, entrapped powders and oxides are a possibility. Even though residual powders reflect sub-optimal AM deposit conditions, for coating purposes, these AM deposits are acceptable because of providing full base material coverage.

2.2 Microstructural Appearance

Figure 4 shows a set of optical macrographs revealing AM deposits down to base materials. Both AM top surface and AM deposit-base material interface exhibit the characteristic pseudo-sinusoidal profile associated with a crosshatched deposition pattern. Specifically, it shows that unknown concentrations of base material have been melted with AM deposits. Additionally, the observed preferential etching on the UNS G41400 steel, UNS S41000, and UNS S17400 stainless steels reveals HAZs below the AM deposits. On the UNS S32750

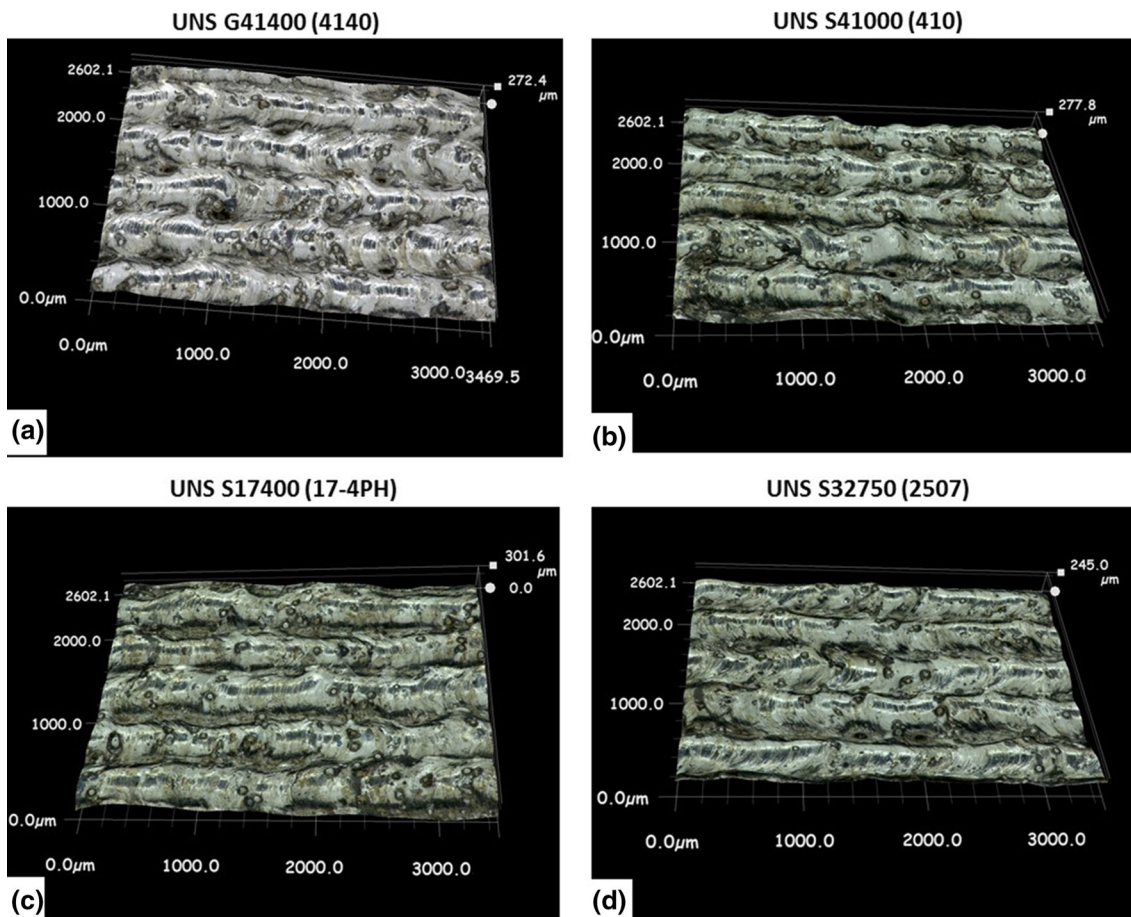


Fig. 3 3D topological images of AM deposits on (a) UNS G41400 (4140), (b) UNS S41000 (410), (c) UNS S17400 (17-4PH), (d) UNS S32750 (2507). Note the thicker AM deposit on the UNS S17400 stainless steel caused by a lower scan speed (600 vs. 800 mm/min)

steel, the HAZ is not as distinct, yet unlikely detrimental due to the absence of martensitic transformation (Fig. 4). For all test samples, the AM deposit varies in thickness between 330 and 500 μm at peaks, and between 225 and 420 μm at valleys. In comparison, the HAZ is thinner with its characteristics dependent upon base materials and process application variables. Variations in AM deposit thickness validate that the powder deposition process was not as stable as expected. Considering thickness between 225 and 420 μm at valleys and powder particle diameters between 45 and 70 μm , the whole AM deposit is only 3-9 powder particles thick. When putting the results of Fig. 4 into perspective, it appears that the AM deposition process has been pushed to limits, where unstable flow streams have become new norm.

Figure 5 shows two complementary magnified views of the AM—base material interface on the UNS S32750 steel. In contrast to the other alloys, 20-30 μm voids were found at the apex of the AM deposit-base material interface at a frequency of about 0.2 void/mm for test samples with a deposition rate of 800 mm/min (Fig. 5a). For selective laser melting (SLM), such voids have been the subject of investigations, particularly by Li et al. (Ref 17). These authors have attributed voids to laser beam variables not being optimized, high powder oxygen content, and a lack of hatch pattern overlap. If these explanations are extended to DED and this investigation, oxygen's effect on wetting phenomena and a greater occurrence of voids, as recognized by Li et al. (Ref 17), would apply more to the

UNS S32750 steel due to its more protective and stable oxide film. However, no such evidence was found, and in all indications the residual powder observed in Fig. 3 is largely remelted upon subsequent passes. Figure 5(b) is a higher-magnification view that shows dark features within an AM deposit. Note that these features also form near-parallel lines with distinct orientations. To those familiar with rapid solidification, these are classic columnar grains and dendritic interfaces. These dark features indicate where the last liquid solidified and where shrinkage due to liquid-to-solid transformation gave rise to microporosity. Shrinkage microporosity along columnar and dendrite arms are typical of AM deposits (Ref 11, 14).

Figure 6 shows SEM secondary electron (SE) images of the AM deposit-base material interface. The SE images for UNS G41400 (Fig. 6a), UNS S41000 (Fig. 6b), and UNS S17400 steels (Fig. 6c) indicate that the base material melted. All three micrographs reveal the following: (1) a curved and pseudo-circular interface directed toward the cooling direction (i.e., upward), (2) shaded bands in the fused zone inferring that some base material was transferred into the melt prior to rapid solidification, and (3) a fine dendritic substructure also aligned with the cooling direction. Complementarily, Fig. 7 presents a higher-magnification micrograph of the UNS N06625 AM deposit about 50 μm above this interface, where a fine columnar inter-dendritic microstructure is confirmed (Ref 11, 14). Estimates of solidification cooling rates are well known

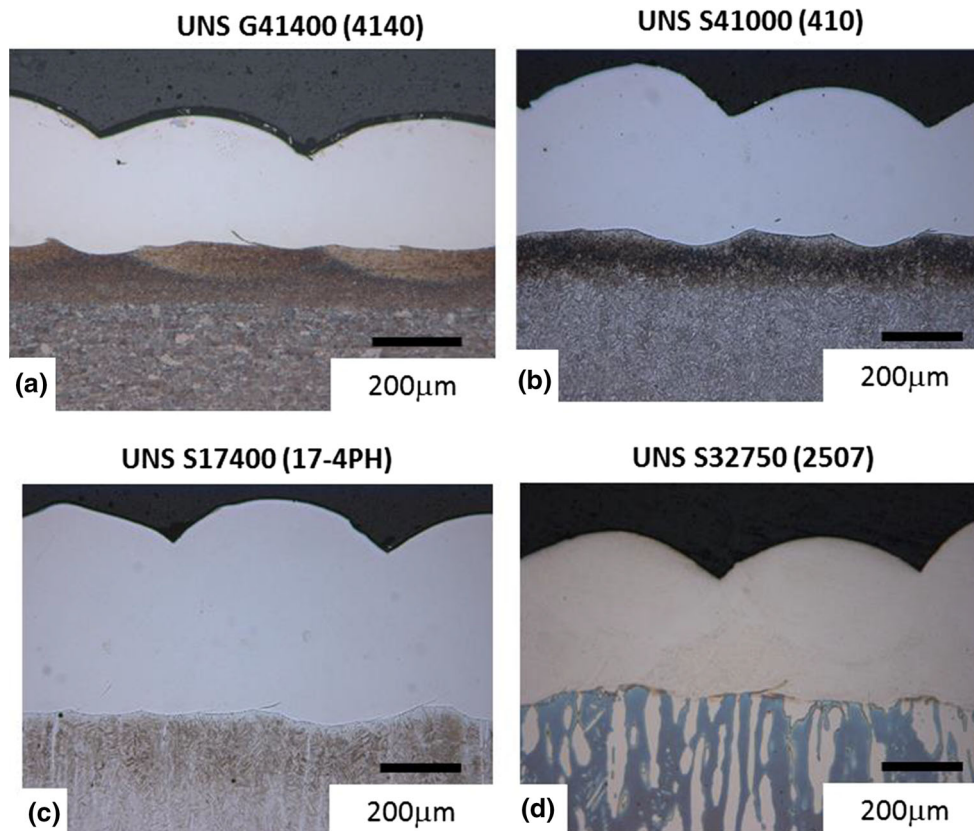


Fig. 4 Etched cross section micrographs for (a) UNS G4140 (4140), (b) UNS S41000 (410), (c) UNS S17400 (17-4PH), and (d) UNS S32750 (25Cr). Note the AM deposit provides full base material coverage and has induced heat-affected zones of various depths, depending upon base materials

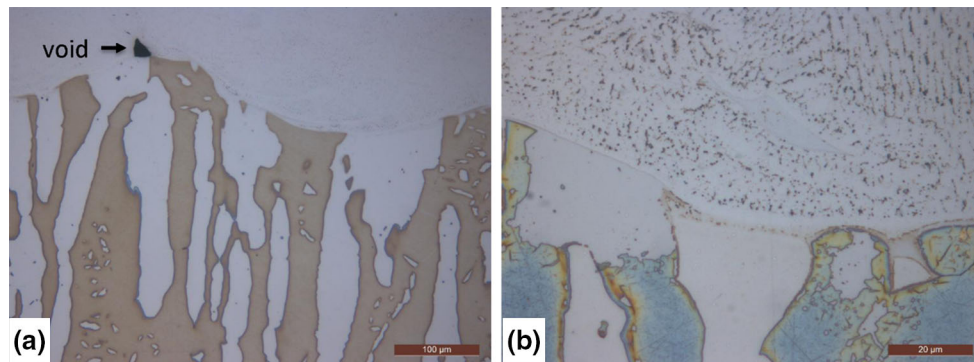


Fig. 5 Optical micrograph of the AM deposit-base material interface, with indications of lack of wetting and melting. Note the presence of a $\sim 20 \mu\text{m}$ void in (a) at the apex of the base material, and dark features in the AM deposit on (b) revealing the solidification structure, including shrinkage microporosity

and have been attempted for fine dendritic AM structures (Ref 11). As in the previous investigation with identical AM parameters (Ref 11), yet a different austenitic powder, dendrite-arm spacing is about $2 \mu\text{m}$. Consequently, cooling rates during solidification appeared to be between 1000 and $4500 \text{ }^\circ\text{C/s}$ (Ref 11). Within the dendritic microstructure, shrinkage microvoids are confirmed along the dendritic growth direction. Most inter-dendritic microvoids are spherical and based on their scale are not interconnected (Ref 11, 14). It follows that the deposited microstructure would thus not impair surface properties, especially protection against corrosion.

In the UNS G41400 and UNS S41000 steel HAZs (Fig. 6), the microstructure is predominantly comprised of fine martensite laths formed by prior-austenite lattice shear mechanism. This fine martensite has been insignificantly tempered by subsequent laser scans and may be related to fast heating and cooling cycles, in rates over $1000 \text{ }^\circ\text{C/s}$. This martensite is also characteristically associated with crack-susceptible alloys, especially by mechanisms of hydrogen embrittlement, chloride stress-corrosion cracking, and sulfide-stress cracking (Ref 9). In regions away from the AM deposit-base material interface, the fine martensite laths are progressively replaced by a coarser,

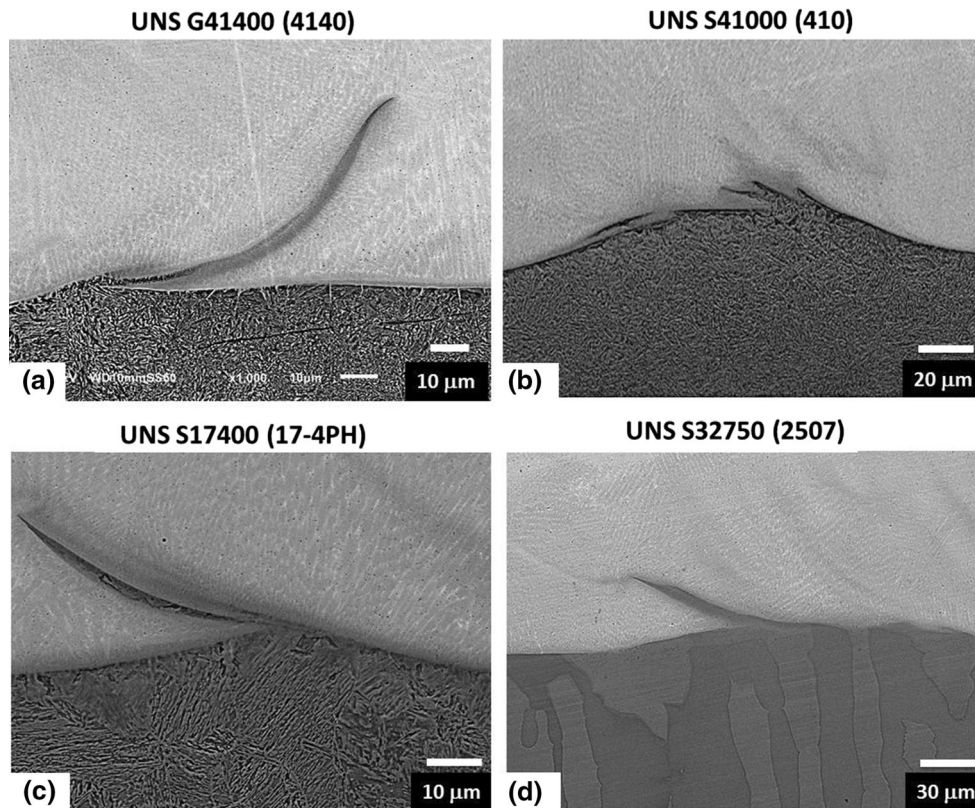


Fig. 6 Interface microstructures of (a) UNS S41400, (b) UNS S41000, (c) UNS S17400, and (d) the UNS S32750

UNS N00625 (625)

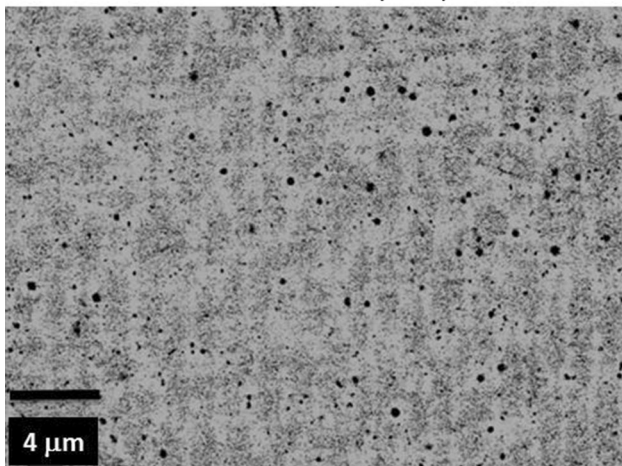


Fig. 7 UNS N00625 AM deposits at high magnification revealing fine dendritic microstructures with submicron voids attributed to solidification shrinkage

thereby more tempered martensite with ferrite and carbides. Correspondingly, the microhardness decreases, eventually leveling off near 250 HVN, the base material hardness value. In the UNS S17400 stainless steel (Fig. 6c), the HAZ microstructure is equally fine. Compared to the UNS S41000 steel, the martensite in the UNS S17400 steel contains less carbon, while the elemental partitioning leads to increased fraction of retained austenite and unresolvable carbides (Ref 18). The corresponding microstructure was consequently

predicted to be softer than in the UNS S41000 stainless steel, yet still cracking-susceptible as per the NACE MR0175/ISO15156 balloted environmental limits (Ref 9, 19). In the UNS S32750 stainless steel (Fig. 6d), the microstructure is largely unchanged, consisting of austenite and ferrite, a microstructure that is least susceptible to cracking in corrosive environments. As additional observation, deleterious phases such as sigma phase, to which sensitization is associated, are absent. The same observation can be extended to any other time-dependent and diffusion-controlled intermetallic phases that are found on TTT and CTT diagrams of super-duplex stainless steels.

2.3 Microhardness Profiles

Figure 8 shows repeated microhardness profiles from top of AM deposits down to base materials. For reference, base material hardness values were 250 HVN for both UNS G41400 and UNS S41000, 320 HVN for UNS S17400, and 270 HVN for UNS S32750. Microhardness within AM deposits consistently averaged 300 HVN did not depend on base materials and never decreased below the base material hardness value. For all alloys, the microstructures are harder in the HAZ, including for the UNS S32750 super-duplex stainless steel. In UNS G41400 and UNS S41000 steels, the HAZ hardening is more prominent, with the microhardness reaching 650 HVN and 550 HVN, respectively. These values are about twice greater than for the base material, indicating the martensite of the HAZ has been negligibly tempered (Fig. 8a and b). The HAZ in these alloys is approximately 100 μm thick, as already revealed by the darker sublayer in Fig. 4. In the UNS S17400 steel, the hardening is relatively moderate, as shown by Fig. 8(c). Correspondingly,

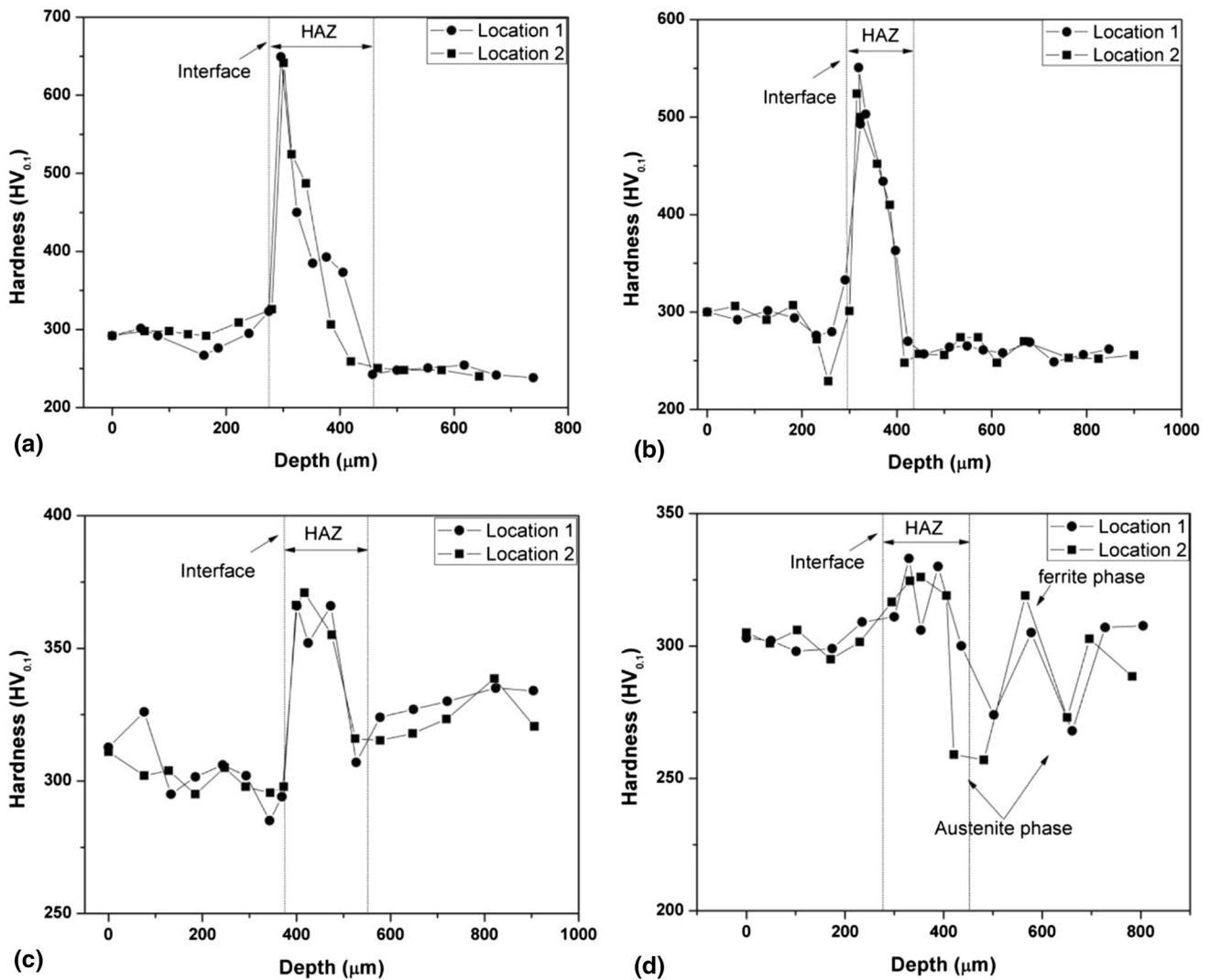


Fig. 8 Microhardness profiles for (a) UNS G41400, (b) UNS S41000, (c) UNS S17400, and (d) UNS S32750. In all cases, some hardening is observed close to the AM—base material interface

the HAZ thickness also averages 100 μm . Microhardness peaked at 375 HVN and thus only exceed by 25% that of the base material. The lesser hardening in the UNS S17400 steel can be rationalized by its low carbon percentage. By the 1970s, the hardness of as-quenched martensite was confirmed to be primarily related to carbon percentage. During rapid cooling, carbon atoms are trapped at octahedral interstitial sites of the martensite BCT structure, causing the lattice to also distort, and overall creating a hard and brittle microstructure (Ref 18). Unlike other alloying elements also in steels, carbon mainly influences tempering and retained austenite content (Ref 18). Common alloying elements, such as chromium, molybdenum, and nickel, influence kinetics of tempering, characteristically delaying the martensite decomposition to ferrite and carbides, as seen in the TTT and CTT diagrams (Ref 18, 19). When comparing the maximum microhardness values herein reported to that in the literature for the as-quench condition (Ref 18), microhardness indicates that no measurable tempering due to subsequent laser scan took place, as was already inferred from the microstructures. Based on transformation diagrams (Ref 18), the martensite structure is retained after cooling time of several seconds, a time much longer than any typical AM laser

scans (Ref 18, 19). Cooling rates in the as-solidified microstructures are in the order of 1000 $^{\circ}\text{C}/\text{s}$, a value arguably extendable to the HAZ, yet suggesting cooling times no more than seconds for the HAZ, for which the applicability of CTT diagrams is questionable. In contrast to the UNS G41400, UNS S41000, and UNS S17400, the microhardness is invariant across the HAZ of the UNS S32750 stainless steel. As anticipated, the austenite is softer (e.g., ~ 250 HVN) relative to the ferrite (~ 320 HVN) (Ref 20). In the UNS S32750 stainless steel, some secondary hardening can be detected in the AM deposit close to the HAZ. This hardening is likely due to some slight dilution (mixing), as further examined in the next section.

Alloy 625 overlay provides corrosion resistance in almost all environment. Heat-affected zone (HAZ) of UNS G41400, UNS S41000, and UNS S17400 stainless steels shows higher hardness than the acceptable values per NACE MR0175/ISO15156 for monolithic material. Material with higher hardness may crack under stress when exposed to corrosion fluid. This prohibits the application of repair process for some oil field applications however protective 625 alloy overlay allows its application on service tools after fit-for-service qualification testing.

Base material: UNS S32750 (2507)

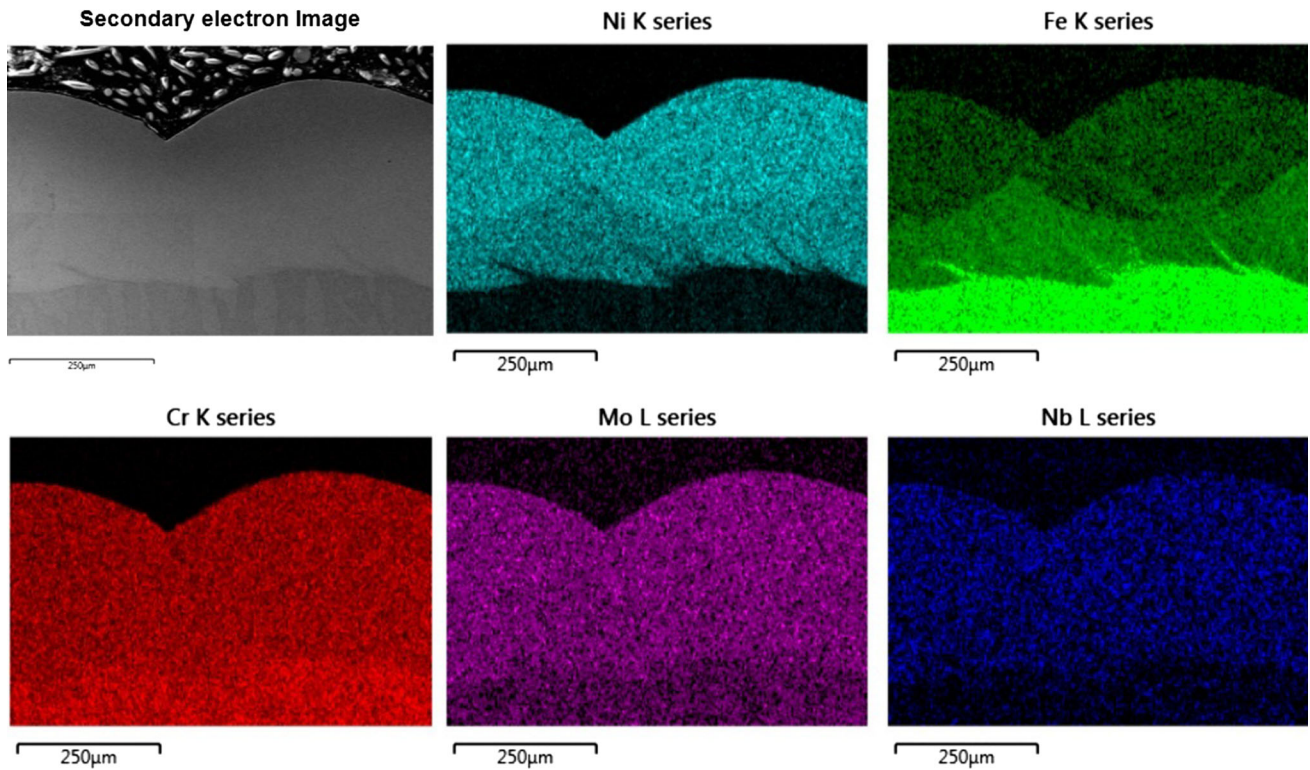


Fig. 9 Secondary electron image and EDS elemental maps for the AM deposit produced on UNS S32750

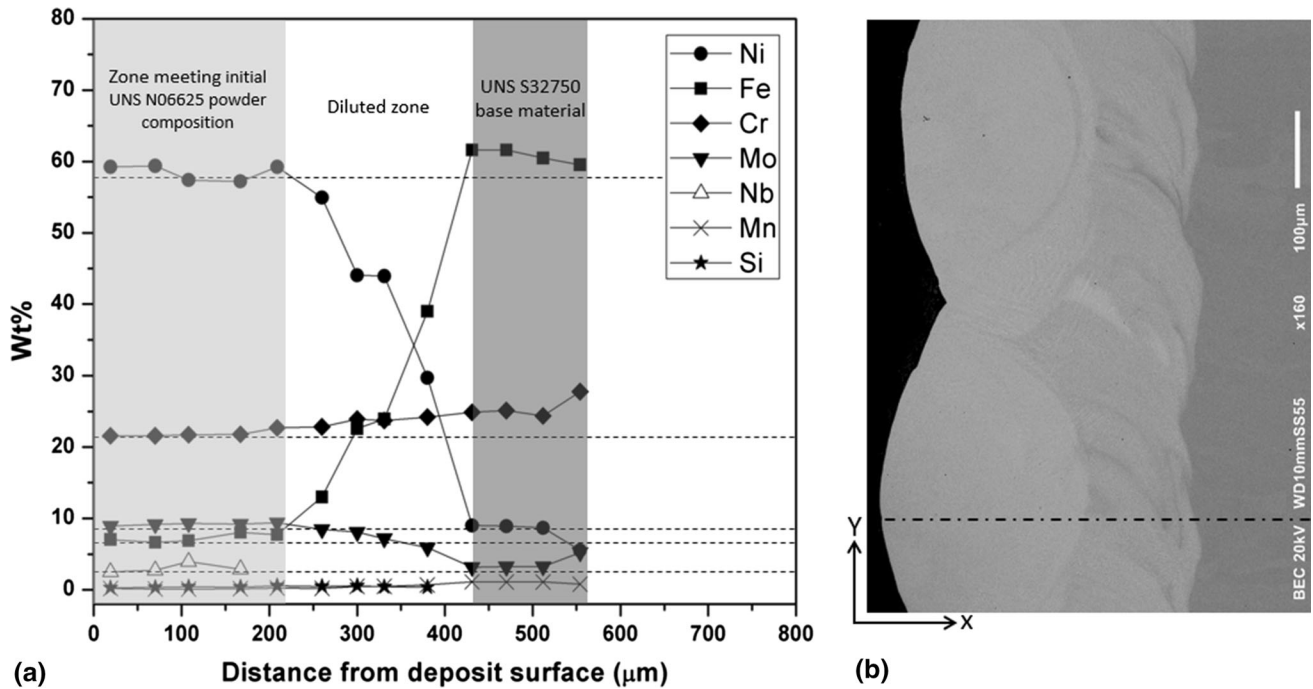


Fig. 10 Elemental distribution (a) across a 625 deposit sample on the UNS S32750 super-duplex stainless steel. The EDS scan line was conducted as shown by the dashed line on the right microstructure (b)

2.4 Compositional Analyses

Figure 9 shows typical secondary electron image and EDS elemental maps for the UNS S32750 AM test sample examined

in Fig. 3-6. Among all elements in UNS S32750 and UNS N06625, only the elemental maps for nickel (Ni), iron (Fe), chromium (Cr), molybdenum (Mo), and niobium (Nb) are

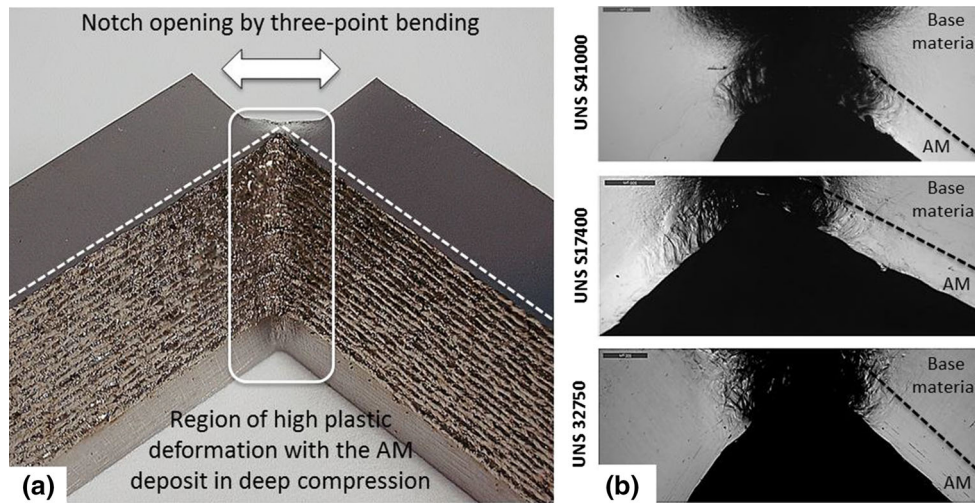


Fig. 11 Overview of a bend test sample of UNS S17400 with UNS N06625 AM deposit, along with 3 optical macrographs showing some significant plasticity developing during bend testing, but no interfacial cracking or AM deposit delamination

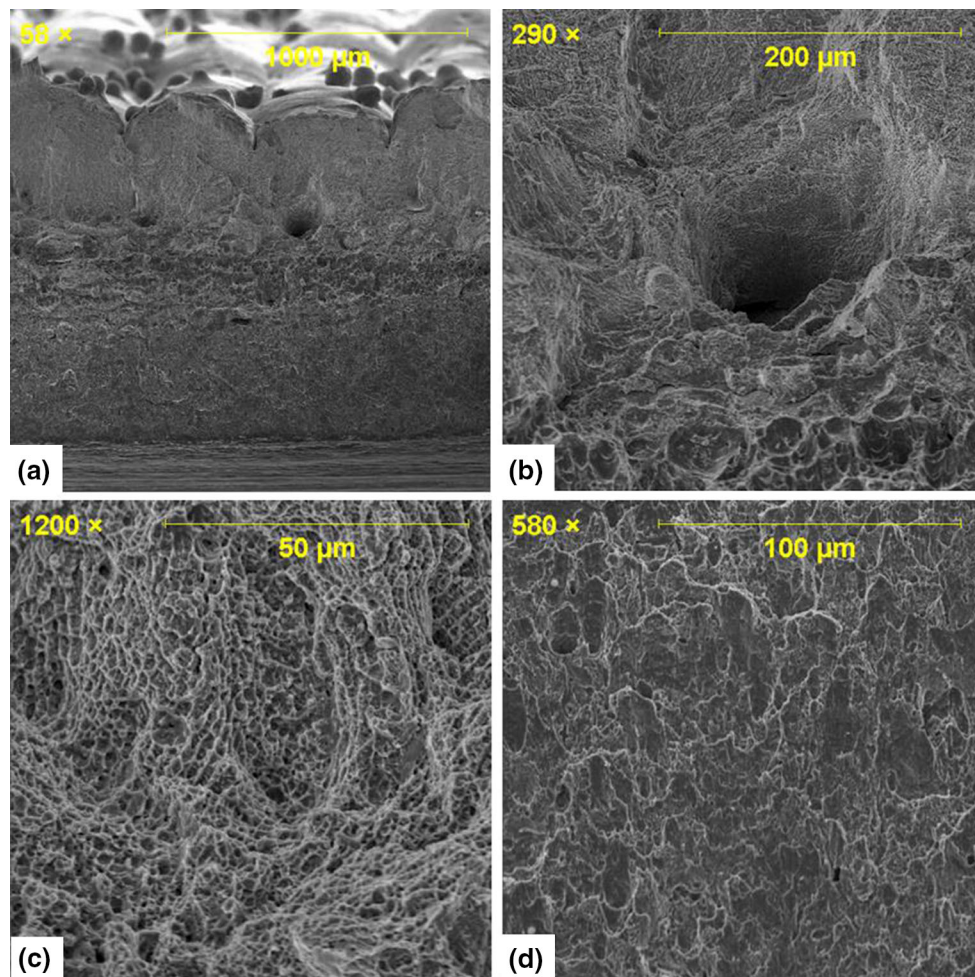


Fig. 12 SEM fractographs (UNS S17400) depicting a 100- μm diameter void along the AM deposit-base material interface, an AM deposit with fine dendritic and ductile microstructure, and the absence of preferential cracking along the AM deposit-based material interface

included because these are critical elements contributing to both corrosion resistance and hardening. Among all EDS compositional maps, the iron distribution is more descriptive, showing distinct zones corresponding to consecutive AM layers. Fig-

ure 9, therefore, validates the presence of dilution (mixing) between base material and powder feed. Specifically it reveals that the iron concentration increased in the very first layer of the AM deposit, whereas the nickel concentration decreases. The

observed increased iron concentration in Fig. 9 also appears to correlate with the slightly greater hardness observed in Fig. 8(d) for the UNS S32750 stainless steel.

Complementary EDS line scans (Fig. 10) further reveal that the upper layer in the AM deposit fully meets the compositional requirements of UNS N06625. In Fig. 10, the AM deposit is up to 440 μm thick, as indicated by the dashed line in Fig. 10(b) (initiated 10–20 μm below the top surface). Approximately half (i.e., $\sim 220 \mu\text{m}$) is indistinguishable in composition from the UNS N06625 powder. Correspondingly, the zone where base material and powder feed are mixed and cause dilution is revealed where chemical composition deviates from original powder composition (dashed lines in Fig. 10a). This zone is also 220 μm thick and fairly well highlighted by the contrast change in the SEM image (Fig. 10b). For this upper layer with UNS N06625 composition (no dilution), the PREN value calculated per the NACE MR0175/ISO15156 formula (Ref 9) using the EDS measurements indicates values in excess of 50, which is greater than that of all stainless steels. Since similar observations applied to other AM deposits, additional EDS line scans have not been included. The conclusion that the PREN of top AM deposit is approximately 50 may be a generalization. Under a different set of AM process conditions such as a higher heat input, the cooling would be slower, perhaps lesser residual powder would stay at surface, while more dilution that can be associated with a lower PREN would be expected. In this hypothetical scenario, PREN reduction would be most noticeable on the leaner alloy, that is the UNS S41000, and least noticeable on the high-chromium alloys, i.e., the UNS S32750 super-duplex stainless steel. This last statement, though speculative, would require a lot more analyses for verification and validation and is of limited relevance to this investigation.

2.5 Bend Testing

To ascertain that the AM deposits are at least as ductile as the base materials and therefore not prone to preferential cracking, bend testing was conducted per the experimental procedure depicted in Fig. 11. Not indicated, but measured after completing the bend tests, were actual distances between tips of notches and AM deposit-base material interfaces. These were confirmed to vary between 1100 and 1550 μm below the AM deposit top surface, indicating the notches were still distant from AM deposit and the HAZ as per the previously reported thickness values. The stress-state in the HAZ was therefore not primarily in tension, as originally expected, but in compression. Due to a test sample shortage, the UNS G41400 steel was not bend tested despite this alloy presenting the greatest concern due to its HAZ hardness. Overall, repeated bend testing on the stainless steels did not reveal interfacial cracking, including delamination, in contrast to bend tests with thermal spray or electroplated test samples (Ref 12). On the 3 optical images of Fig. 11, many deformation fringes across both base material and AM deposit can be seen and are further evidence of overall ductility, particularly for the AM deposits. In the selected test configuration, cracking was observed only within the base materials, not along the AM deposit-base material interface (HAZ side), where the microstructure is hardest. Note that the UNS S17400 stainless steel test samples in Fig. 11(b) were less bent than the other test samples because of its greater hardness (i.e., 320 HNV). Bend testing was conducted up to full separation. Full separation of the bend test samples was more

difficult to produce in the AM bend testing samples of the UNS S32750 super-duplex stainless steel.

Figure 12 shows SEM micrographs of the fractured surface for the UNS S17400 test sample of Fig. 11. Figure 12(a) and (b) both indicates a relatively large void along the AM deposit-base material interface. This void has similarities to the void of Fig. 5, even though voids were not evident in examinations of cross sections for the UNS S17400 AM samples. The specific size and position of this void along the AM deposit-base material interface indicate that this void is due to a lack of overlap between fused lines (unlike the smaller solidification shrinkage voids). Note that the fracture surface in the region above the void is highly tortuous, an indication of the very ductile plastic behavior of UNS N06625. Figure 12(c) shows a high magnification view of the AM deposit fracture surface. As seen earlier, the observed microstructure is particularly fine, revealing a dendritic substructure similar to previous investigations (Ref 11, 14). The microstructure below the base material (correspondingly in the HAZ) is coarser, thus indicating a more brittle microstructure despite being transgranular and exhibiting smeared or angled dimples (Fig. 12d). Figure 11 and 12 are the perfect illustrations that bend testing did not cause either interfacial cracking (delamination) or obvious cracking in the HAZ (none in Fig. 11, or other independent observations) and as such validates DED laser powder as a promising repair for ferrous parts.

3. Conclusions

The DED laser deposition of UNS N06625 powder on martensitic stainless steel UNS G41400, UNS S41000, precipitation-hardened martensitic stainless steel UNS S17400, and super-duplex stainless steel UNS S32750 has shown beneficial results for applications onto oil field ferrous parts. Compared to well-established industrial cladding processes, DED by laser powder deposition is proven to be well suited to minimize base material melting (dilution), reduce the extents of heat-affected zones, and overall lead to part in-service property improvements. In this investigation, through microhardness indentation surveys, metallographic examinations, EDS compositional maps, and simple bend testing, it was established that dense, ductile, and crack-free AM deposits with fine dendritic solidification structures near 300 HVN can be achieved on all four tested steels. All AM deposits were found to be within 330 and 500 μm thick, with approximately half their thickness diluted with the base material and conveying no negative consequences on AM hardness. The top surface also fully achieved the compositional requirements of UNS N06625. Due to rapid cooling, the AM deposit microstructures were consistently fine (2 μm dendrite-arm spacing) with inconsequential submicron porosity at inter-dendritic spaces. Despite a controlled heat input, the heat-affected zones exhibited high hardness, quite above-normally accepted hardness values on UNS G41400, UNS S41000, and UNS S17400 stainless steels for typical oil field applications. For UNS S32750, microhardness was unnoticeably changed, therefore not restricting AM as a repair process for oil field parts. With the three steels subject to martensitic stainless steels, the HAZ hardened layer is approximately 100 μm thick. In contrast to UNS S32750, some martensitic-type hardening as thick as 100 μm was found in

both the UNS S41000 (410) and UNS S17400 stainless steels. Though suspected to be inconsequential in the use within service tools, this hard layer (350-650 HVN depending upon the alloys) remains a major concern for equipment designed for corrosive service and would require its own fit-for-service qualification testing.

References

1. B. Garrett, 3D Printing: New Economic Paradigms and Strategic Shifts, *Glob. Policy*, 2014, **5**(1), p 70–75
2. C. Weller, R. Kleer, and F.T. Piller, Economic Implications of 3D Printing: Market Structure Models in Light of Additive Manufacturing Revisited, *Int. J. Prod. Econ.*, 2015, **164**, p 43–56
3. E. Atzeni and A. Salmi, Economics of Additive Manufacturing for End-Usable Metal Parts, *Int. J. Adv. Manuf. Technol.*, 2012, **62**(9), p 1147–1155
4. T.T. Wohlers, *Additive Manufacturing and 3D Printing State of the Industry, Annual Worldwide Progress Report*, Wohlers Associates, Fort Collins, 2013
5. J.P.K. Peter, Mercelis, Residual Stresses in Selective Laser Sintering and Selective Laser Melting, *Rapid Prototyp. J.*, 2006, **12**(5), p 11
6. T. Amine, J.W. Newkirk, and F. Liou, An Investigation of the Effect of Direct Metal Deposition Parameters on the Characteristics of the Deposited Layers, *Case Stud. Therm. Eng.*, 2014, **3**, p 21–34
7. J. Ruan, T.E. Sparks, Z. Fan, J.K. Stroble, A. Panackal, and F. Liou, A review of layer based manufacturing processes for metals, *Solid Freeform Fabrication Symposium*, R.H.C.D.L. Bourell, J.J. Beaman, K.L. Wood, and H. Marcus, Ed., University of Texas Press, Austin, 2006, p 13
8. M. Marya, V. Singh, Y. Lu, J.-Y. Hascoet, and S. Marya, Transition Microstructures and Properties in the Laser Additive Manufacturing Repair of Monel K-500 (UNS N05500) and Toughmet 3 AT (UNS C72900), *The Minerals, Metals and Materials Society (TMS) 2015*, 2015
9. ANSI/NACE MR0175/ISO 15156, *Petroleum and Natural Gas Industries—Materials for Use in H₂S-Containing Environments in Oil and Gas Production*, NACE, Houston, 2015, p 164
10. J. Bellarby, Chapter 8 Material selection, *Developments in Petroleum Science*, B. Jonathan, Ed., Elsevier, New York, 2009, p 433–472
11. M. Marya, V. Singh, S. Marya, and J.Y. Hascoet, Microstructural Development and Technical Challenges in Laser Additive Manufacturing: Case Study with a 316L Industrial Part, *Metall. Mater. Trans. B*, 2015, **46**(4), p 1654–1665
12. ASTM B571, *Standard Practice for Qualitative Adhesion Testing of Metallic Coatings*, American Society of Testing and Materials, West Conshohocken, 2013, p 4
13. S.M.J.Y. Hascoët, M. Marya, and V. Singh, Challenges in the Development and Implementation of Additive Manufacturing for Industrial Parts, *1st International Conference on Progress in Additive Manufacturing*, Y.W.Y., C.C. Kai, T.M. Jen, A.W. Teong, Ed., 2014, p 133–139
14. M. Marya, S. Marya, V. Singh, P. Sadik, and J.-Y. Hascoet, On the Laser Additive Manufacturing Repair of UNS S41000, UNS S17400 and UNS S32750 by UNS N06625, *Materials Science and Technology (MS&T) 2015* (Ohio), MS&T15, 2015, p 109
15. J.Y. Hascoet, K.P. Karunakaran, and S. Marya, Additive Manufacturing Viewed from Material Science: State of the Art and Fundamentals, *Materials Science Forum*, vol 783–786, 2014
16. K.C. Mills and B.J. Keene, Factors Affecting Variable Weld Penetration, *Int. Mater. Rev.*, 1990, **35**(1), p 185–216
17. R. Li, Y. Shi, Z. Wang, L. Wang, J. Liu, and W. Jiang, Densification Behavior of Gas and Water Atomized 316L Stainless Steel Powder During Selective Laser Melting, *Appl. Surf. Sci.*, 2010, **256**(13), p 4350–4356
18. G. Krauss, *Steels: Processing, Structure, and Performance*, ASM International, Materials Park, 2015
19. O. Grong, *Metallurgical Modelling of Welding*, 2nd ed., Maney Publishing, Leeds, 1997
20. S. Atamert and J.E. King, Elemental Partitioning and Microstructural Development in Duplex Stainless Steel Weld Metal, *Acta Metall. Mater.*, 1991, **39**(3), p 273–285